6 Single Component, Multiphase (SCMP) LBM

In the previous chapter we demonstrated that LBM is useful for simulating the flow of a single fluid. The true strengths of LBMs however lie in their ability to simulate multiphase fluids. Both single and multi-component multiphase fluids can be simulated. 'Component' refers to a chemical constituent such that a 'single component' (say H_2O) multiphase system would involve the liquid and vapor phases of water. These are particularly rich systems to consider as surface tension, evaporation, condensation, and cavitation are possible. Liquid-vapor behavior in partially saturated porous media can be simulated. In contrast, a multi-component system can consist of separate chemical components such as oil and water; such systems have been studied more extensively because of their economic importance. For example, Darcy's law-based relative permeability concepts for multicomponent oil/water-like systems have been investigated using LBM (Buckles et al. 1994; Soll et al. 1994; Martys and Chen, 1996; Langaas and Papatzacos, 2001).

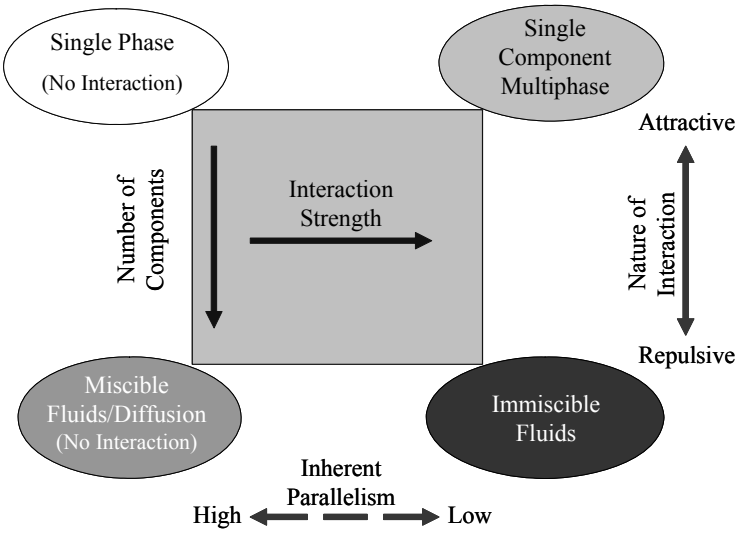

Figure 38. Conceptual framework for LBM models.

Figure 38 gives a conceptual framework for thinking about the various LBM models to be considered in this book. At the upper left we have the simple single fluid models discussed in the last two chapters: these involve a single chemical component whose molecules are not subjected to any 'long-range' interaction forces. Adding a long-range attractive force makes phase separation into a liquid and its own vapor possible as discussed below (upper right, single component multiphase).

If we add a second chemical component, we have the possibility of simulating completely miscible fluids (basically chemical solutions) in the absence of long range interactions (lower left), and completely immiscible fluids (oil and water for example) when there are long range repulsive interactions (lower right). Finally, note that the widely acclaimed inherent parallelism of LBM is lost when long range interactions are included.

This chapter focuses on Single Component Multiphase (SCMP) models. Early examples of lattice gas SCMP models can be found in Rothman (1988) and Appert and Zaleski (1990). The lattice Boltzmann implementation of these models began with Shan and Chen (1993, 1994). There are also so-called ''free energy'' approaches proposed by Swift et al. (1996), and ''finite density'' models that use the Enskog equation for dense gases (Luo 2000; He and Doolen 2002). Zhang and Chen (2003) have also proposed an approach based on tracking an energy (temperature) component. Such finite density or energy models seem to hold the key to the ultimate development of the LBM for practical applications due to the more realistic and consistent treatment of the equation of state that preserves the essential (molecular) physics of the process. Here we work with the Shan and Chen (1993, 1994) model extended for solids interactions. Although this model has numerous shortcomings, it is exceptionally versatile, and problems that have long defied quantitative treatment can now be examined.

First we recall basic physical chemistry theory relevant to these models. Then we provide details on incorporating long-range forces into the LBM model and on the resulting LBM equation of state. The determination of surface tension in the model is illustrated. Simulation of homogeneous and heterogeneous cavitation with the model are presented. Then interactions with surfaces are included and contact angles, capillary rise, adsorption, and capillary condensation are discussed.

The principal distinguishing characteristic of single component multiphase LBMs is the incorporation of an attractive force between fluid 'particles'. This notion is part of the foundation for the famous van der Waals equation of state, which we now review.

6.1 Non-ideal Equation of State

The 'ideal' or 'perfect' gas law characterizes the behavior of gases at low density. Such gas laws are also known as Equations of State (EOS). The ideal gas law is commonly written as

$$PV = nRT \text{ or } P = \frac{nRT}{V} \tag{54}$$

where

- P is pressure (a*tm*)
- V is volume (L)
- n is number of mols
- R is gas constant (0.0821 $L\ atm\ mol^{-1}\ K^{-1}$)
- T is temperature (K).

$V_m = V/n$ is the volume occupied by one mol of substance. The gas laws can be re-written to eliminate the number of mols n

$$P = \frac{RT}{V_m}. \tag{55}$$

Eqs. (54) and (55) are linear relationships between pressure and density (which is proportional to n/V).

The van der Waals EOS was developed to account for behaviors observed in real gases while retaining conceptual simplicity. It is given by

$$P = \frac{nRT}{V - nb} - a\left(\frac{n}{V}\right)^2. \tag{56}$$

The second term on the right accounts for attractive forces between molecules. Note that because a, n, and V are all positive, this term results in a reduction of the pressure relative to that of a perfect gas.

The $-nb$ term in the denominator accounts for the non-negligible volume of molecules. If the 'hard sphere', closest packed volume of one mol of molecules is b, then the minimum volume that can be occupied by n mols of molecules is nb. As the pressure increases, the volume of the gas V may approach nb. This will cause the denominator to approach zero and the pressure will rise very rapidly, effectively preventing further compression.

The van der Waals gas law can also be rewritten in terms of the molar volume:

$$P = \frac{RT}{V_m - b} - a\left(\frac{1}{V_m}\right)^2 . \tag{57}$$

6.1.1 P–V_m, and P–ρ Presentations

The gas laws are typically presented graphically in one of two formats: in P–V space, pressure is plotted against volume while in P–ρ space, pressure is plotted against density. P–ρ plots are more intuitive and useful in general, but there is one very important manipulation that requires use of P–V plots.

Figure 39 shows the P–V_m plot for CO_2. In this plot, the perfect gas law is non-linear (like $y = 1/x$, because P is inversely proportional to V_m). The van der Waals EOS at various temperatures with parameters a and b taken from Atkins (1978) was used to plot the other curves. Temperatures were selected to illustrate supercritical, critical, and subcritical behaviors. At high temperature ($373K$) CO_2 is supercritical and no distinct liquid and vapor phases can be discerned. As the temperature is decreased, a critical temperature is reached; below this temperature phase separation into liquid and vapor is possible. The key difference in the EOS curves above and below the critical temperature is that above the critical temperature the curves decrease monotonically. Below the critical temperature the curves are no longer monotonic and this allows the coexistence of different molar volumes (different densities) of the substance at a single pressure.

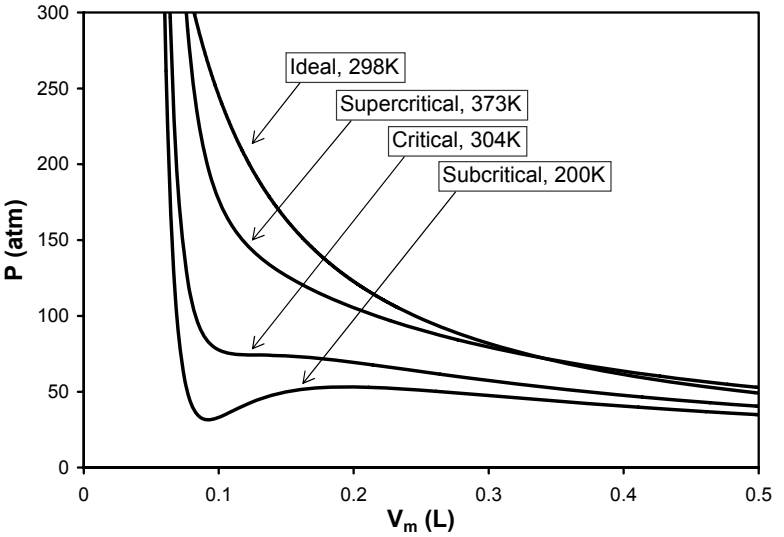

Figure 39. *P–V* plot of perfect and van der Waals equations of state for CO_2. van der Waals constants $a = 3.592\ l^2\ atm\ mol^{-2}$ and $b = 0.4267\ l\ mol^{-1}$ (Atkins, 1978). $R = 0.0821\ l\ atm\ mol\ K^{-1}$.

If we zoom in on a subcritical curve (Figure 40) we see that the EOS is intersected 3 times at the vapor pressure of CO_2 at 293*K*. Projecting the first intersection at small molar volume (high density) down to the *x*-axis gives the molar volume of the liquid. The second intersection is in what is referred to as a 'non-physical' portion of the EOS because the positive slope here indicates that increasing the pressure would cause the vapor to expand. The final intersection gives the molar volume of the equilibrium vapor phase. It is important to note that the vapor pressure applies only to flat liquid-vapor interfaces; we will explore the impact of curvature later.

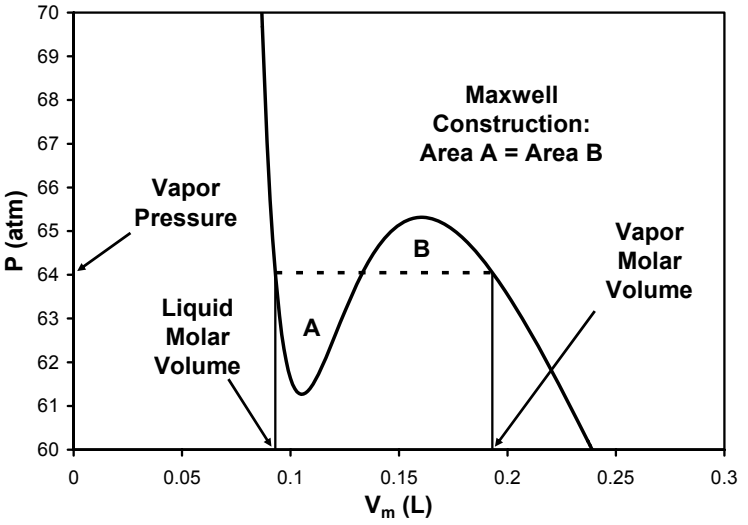

Figure 40. Detail of subcritical EOS for CO_2 illustrating liquid-vapor coexistence (293*K*). The molar volumes of the liquid and vapor and the vapor pressure can be determined from the Maxwell Construction.

6.1.2 Maxwell Construction and its Solution

In the context of LBM, the key reason for using *P*–*V* representations of the EOS is the Maxwell Construction. The Maxwell Construction allows the vapor pressure and the densities of the liquid and vapor phases to be found analytically when a functional form of the EOS is available. Boltzmann (1964/1995) discusses the Maxwell Construction and Figure 40 illustrates its use.

The Maxwell Construction can be stated as

$$\int_{V_{m,l}}^{V_{m,v}} P dV_m = P(V_{m,v} - V_{m,l}) . \tag{58}$$

So the area under the curve (use caution if the EOS goes below P = 0) must equal the area of the rectangle defined by the liquid and vapor molar volumes and the vapor pressure. This is equivalent to specifying that the areas

A and B shown on Figure 40 must be equal. Despite its apparent simplicity, the Maxwell construction can be challenging to solve. One approach is simply to estimate the vapor pressure from the plot. For example, the integral PdV_m where P is given by the van der Waals equation (57) is

$$\int PdV_m = RT\ln(V_m - b) + \frac{a}{V_m}. \tag{59}$$

Based on inspection of the EOS curve in Figure 40, suppose we estimate a vapor pressure of 63 *atm*. For T = 293.15*K* we can estimate $V_{m,l}$ = 0.095 *liters* and $V_{m,v}$ = 0.206 *liters* (by looking at a table or graph of values of $P(V_m)$ for example) and evaluate the integral between these limits to obtain a value of approximately 7.09. For P = 63 *atm* the right hand side of Eq. (58) is 63(0.206-0.095) = 6.99; comparing this with the 7.09 from the left hand side indicates that improvement is possible. Increasing the vapor pressure to 64 *atm* we can estimate $V_{m,l}$ and $V_{m,v}$ = 0.93 and 0.194 *liters* respectively. Then the integral value is 6.45 and the right hand side is 6.46, which is considerably better than the initial guess. Further refinements can be made. We will revisit the Maxwell Construction after the LBM EOS is introduced.

6.1.3 EOS for Water/Water Vapor and $P-\rho$ Presentations

Water is of particular interest to a broad range of scientists and engineers but it is also more complex than can be adequately described by the standard van der Waals EOS. We explore water in some additional detail here and use it to introduce $P-\rho$ plots.

Figure 41 shows the perfect gas and van der Waals equations of state for water at 298K. There are significant differences between the CO_2 and water equations of state. Perhaps most striking is that the curve extends into strong negative pressures. Figure 42 shows the same information plotted as $P(\rho)$. The virtues of such a plot are immediately apparent. The perfect gas law plots as a straight line through the origin and the low and high density (vapor and liquid) portions of the curve are clear and in familiar units.

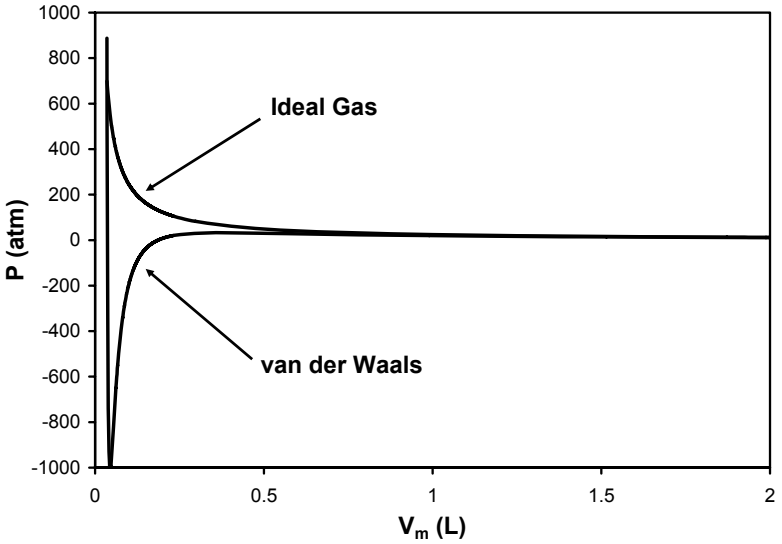

Figure 41. P–V_m representation of perfect and van der Waals EOS for water.

It is also clear however that the van der Waals equation fails to quantitatively reproduce the known density (1000 $kg\ m^{-3}$) of water. Finally, the known compressibility of liquid water is not well matched. Truskett et al. (1999) incorporated directional hydrogen bonds in a model to estimate the water EOS and achieved good success (Figure 43).

One additional feature of the non-linear equations of state discussed here is the bottom of the valley; it is referred to as the *spinodal* and represents the maximum tension that a pure liquid can sustain. So, referring to Figure 43 for example, we can imagine beginning with pure liquid water in a cylinder at its familiar density of 1000 $kg\ m^{-3}$ and then withdrawing a piston that stretches the water to a density somewhat less than 800 $kg\ m^{-3}$. The pressure in the water will follow the EOS and be approximately -2000 *atm*. If the density is reduced beyond the minimum of the EOS curve, the liquid will catastrophically phase separate into liquid and vapor in the process known as *cavitation*. For pure liquids this will occur at the spinodal and is called homogeneous cavitation. Heterogeneous cavitation is much more common and occurs at much lower tension when the structure of the liquid is disrupted by pre-existing bubbles or particles. We will examine both homogeneous and heterogeneous cavitation with LBM below.

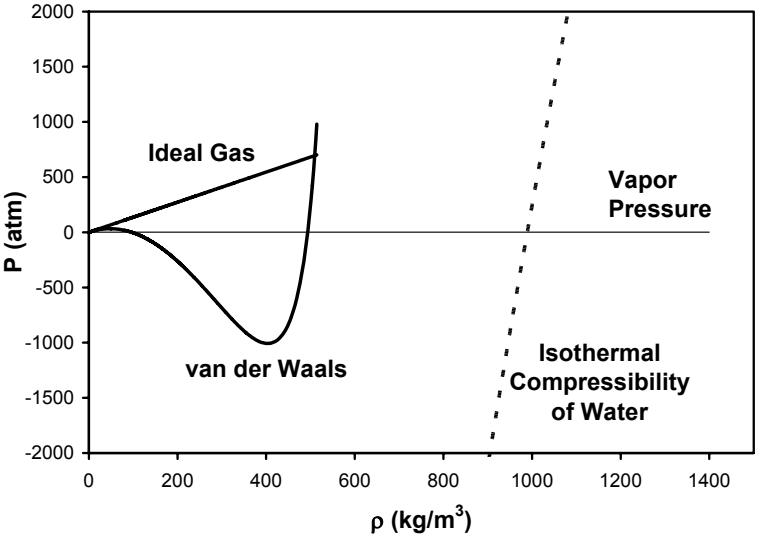

Figure 42. *P–ρ* representation of perfect and van der Waals EOS for water at 298K. There is a gross underestimation of the density of liquid water.

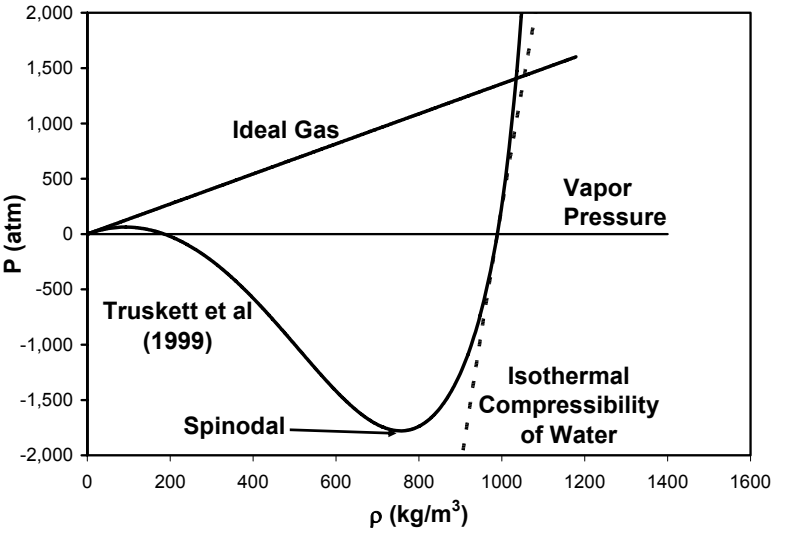

Figure 43. Truskett et al. (1999) EOS for water showing the spinodal. Incorporating directional hydrogen bonding allows good matching of the key features of water behavior.

6.2 Interparticle Forces and their Incorporation into LBM

Lattice Boltzmann models presented thus far in this book were based exclusively on streaming and collision. To simulate multiphase fluids, we need long range interactions between fluid 'particles'. For our purposes interactions with nearest neighbor particle densities f will be sufficient to simulate the basic phenomena of multiphase fluid interactions. For single component multiphase fluids (e.g., water/water vapor) an attractive (cohesive) force F between nearest neighbor fluid particles is needed and, for the D2Q9 model, is induced as follows:

$$\mathbf{F}(\mathbf{x},t) = -G\psi(\mathbf{x},t)\sum_{a=1}^{8} w_a \psi(\mathbf{x}+\mathbf{e}_\mathbf{a}\Delta t,t)\mathbf{e}_\mathbf{a} \tag{60}$$

where G is the interaction strength, w_a is 1/9 for a = {1, 2, 3, 4}, is 1/36 for a = {5, 6, 7, 8}, and ψ is the interaction potential:

$$\psi(\rho) = \psi_0 \exp\left(-\rho_0 \middle/ \rho\right). \tag{61}$$

ψ_0 and ρ_0 are arbitrary constants. This interaction potential is special in that its ''…behavior is consistent with that of an isothermal process...'' (Shan and Chen 1994; see also He and Doolen 2002). According to Shan and Chen (1993), the interaction potential function must be monotonically increasing and bounded. Other forms of the interaction potential are commonly used and include for example $\psi(\rho) = \rho_0[1\text{-}\exp(-\rho/\rho_0)]$ (Shan and Chen 1993; Raiskinmäki et al. 2000 and 2002; Hyväluoma et al. 2004), $\psi(\rho) = \rho$ (Martys and Chen 1996; Pan et al. 2004), and $\psi(\rho) = g\rho_0^2\rho^2/[2(\rho_0+\rho)^2]$ (Qian et al. 1995).

Figure 44 shows the Eq. (61) interaction potential function with $\psi_0 = 4$ and $\rho_0 = 200$. These parameters were selected arbitrarily, but will be used consistently in SCMP LBM simulations in this book for convenience because the model behavior with these values has been explored more thoroughly. $G < 0$ for attraction between particles and the force is stronger when the density is higher. Thus, dense regions (liquid) experience a stronger cohesive force than vapor, which leads to surface tension phenomena.

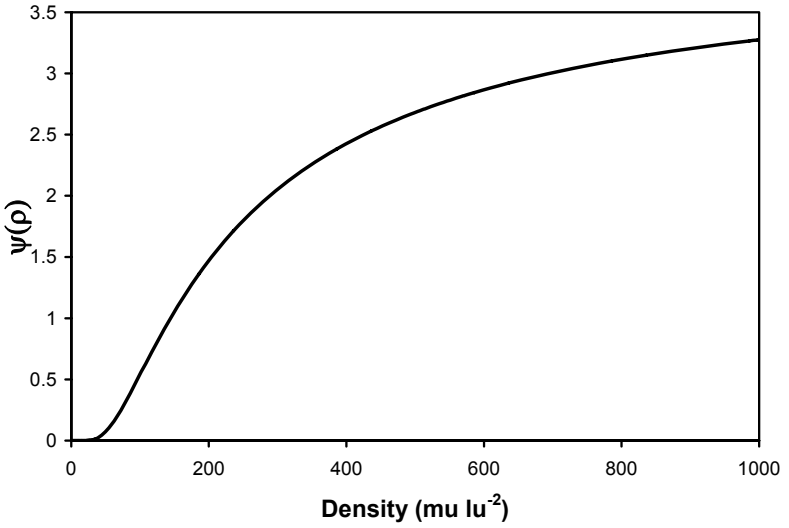

Figure 44. 'Isothermal' interaction potential function of Shan and Chen (1994) with $\psi_0 = 4$ and $\rho_0 = 200$. Other forms of the interaction potential are in common use. We use 2-D densities and pressures throughout the text.

The attractive force is included in the model the same way that gravity was incorporated earlier (Eqs. (45), (46), and (47)).

It is important to note that we have incorporated only the molecular attraction aspect of the van der Waals gas model described above; the repulsive forces that dominate the van der Waals gas model when a gas is compressed to near its 'hard sphere' volume are neglected in this simplest of SCMP models. Enskog developed theory for dense gases that has been incorporated in more advanced LBM models (e.g., He and Doolen, 2002; Martys 2001; Luo 2000; Luo, 1998). Ignoring these effects here has important ramifications for the equations of state of the simulated gases that will be introduced below. At the present time, the ability of LBM to simulate any desired EOS is severely limited. The work of He and Doolen (2002) may hold the key to resolving EOS limitations (and also allow non-isothermal flows) but requires decoupling of velocity and space discretizations and has not been explored. The approach of Zhang and Chen (2003) may be similarly profitable. Nevertheless, the simple Shan and Chen (1993, 1994) model is capable of simulating rich SCMP behaviors includ-

ing surface tension/capillarity, evaporation, condensation, and homogeneous and heterogeneous cavitation.

6.2.1 The SCMP LBM EOS

Application of Eqs. (60) and (61) leads to a non-ideal EOS for the simulated fluids (He and Doolen, 2002):

$$P = \rho RT + \frac{GRT}{2}\left[\psi(\rho)\right]^2 . \tag{62}$$

The first term on the right hand side is the ideal gas law, which applies to the single component, single phase model discussed above. The value of RT is fixed for both the SCSP and SCMP models:

$$RT = \frac{1}{3}. \tag{63}$$

The second term on the right hand side of (62) is the non-ideal part that accounts for the attractive force between the molecules and leads to a reduction in pressure (when $G < 0$) and the non-linear form of the EOS. When G is adequately negative that the EOS is subcritical (non-monotonic), phase separation can occur.

After incorporating RT, Eq. (62) becomes

$$P = \frac{\rho}{3} + \frac{G}{6}\Psi^2(\rho). \tag{64}$$

This is plotted for a series of G values in Figure 45. This EOS is qualitatively similar to the van der Waals EOS and is useful in simulating Laplace Law and capillary phenomena. The lack of a repulsive force in the model however has led to unfortunate (and generally not physically correct) behavior where the liquid phase is actually more compressible than the vapor phase. (The slope $dP/d\rho$ of the curve is lower in the liquid density region than it is in the vapor region.) This does not affect equilibrium liquid-vapor configurations but makes certain types of simulations more challenging and one always needs to be aware of it.

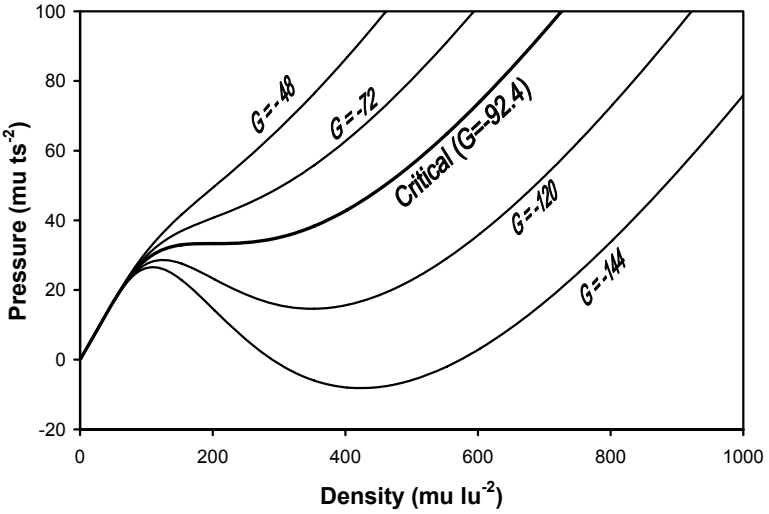

Figure 45. SCMP EOS for $\psi_0 = 4$ and $\rho_0 = 200$ at 5 values of G.

Eqs. (60) and (61) are implemented as follows:

```
// Compute psi, Eq. (61).
for( j=0; j<LY; j++)
  for( i=0; i<LX; i++)
    if( !is_solid_node[j][i])
    {
      psi[j][i] = 4.*exp( -200. / ( rho[j][i]));
    }

// Compute interaction force, Eq. (60) assuming periodic domain.
for( j=0; j<LY; j++)
{
  jp = ( j<LY-1)?( j+1):( 0   );
  jn = ( j>0   )?( j-1):( LY-1);

  for( i=0; i<LX; i++)
  {
    ip = ( i<LX-1)?( i+1):( 0   );
    in = ( i>0   )?( i-1):( LX-1);

    Fx = 0.;
    Fy = 0.;

    if( !is_solid_node[j][i])
    {
      Fx+= WM*ex[1]*psi[j ][ip];
      Fy+= WM*ey[1]*psi[j ][ip];
      Fx+= WM*ex[2]*psi[jp][i ];
```

```
        Fy+= WM*ey[2]*psi[jp][i ];
        Fx+= WM*ex[3]*psi[j ][in];
        Fy+= WM*ey[3]*psi[j ][in];
        Fx+= WM*ex[4]*psi[jn][i ];
        Fy+= WM*ey[4]*psi[jn][i ];
        Fx+= WD*ex[5]*psi[jp][ip];
        Fy+= WD*ey[5]*psi[jp][ip];
        Fx+= WD*ex[6]*psi[jp][in];
        Fy+= WD*ey[6]*psi[jp][in];
        Fx+= WD*ex[7]*psi[jn][in];
        Fy+= WD*ey[7]*psi[jn][in];
        Fx+= WD*ex[8]*psi[jn][ip];
        Fy+= WD*ey[8]*psi[jn][ip];

        Fx = -G * psi[j][i] * Fx;
        Fy = -G * psi[j][i] * Fy;
      }
    }
  }
```

Beware of the assumption about a periodic domain (see the note in the comment at the top of the code snippet). When using boundary conditions, the interaction force must be computed differently at those boundaries because the density is not necessarily continuous across the periodicity then. Hence, the three terms in Eq. (60) associated with nodes across the periodic boundary are unavailable. We find that replacing those three terms with duplicates of the three terms in the other direction (towards the interior of the domain instead of across the boundary of the domain) gives good results.

6.3 Phase (Liquid-Vapor) Separation and Interface Minimization

The preceding model development is enough to simulate phase separation and its dynamics. In Figure 46, we show the results of a simulation initialized with an average density of 200 *mu* lu^{-2} with a random variation incorporated via the 'static' initial condition included in our code. For the standard parameter values ($\psi_0 = 4$ and $\rho_0 = 200$) and ψ function we adopt, this initial density falls on the negatively-sloped, non-physical part of the $G = -120$ EOS (Figure 45) and hence is unstable and leads to phase separation. In this case, the phase separation ultimately leads to a single droplet in a vapor atmosphere. Whether liquid drops or vapor bubbles are formed depends on the total mass in the domain and consequently on the initial density selected.

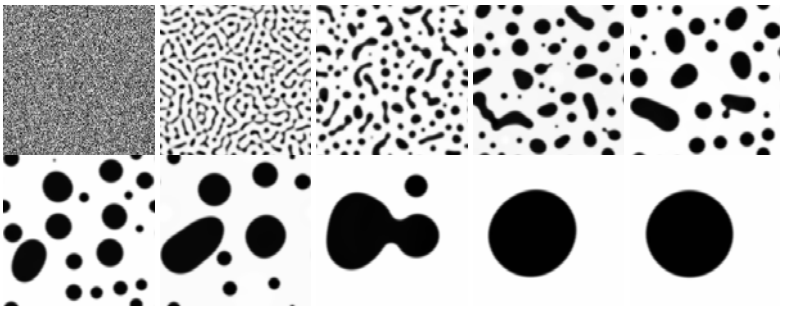

Figure 46. Time series of liquid-vapor phase separation dynamics in a 200×200 lu^2 domain. Gray scale proportional to normalized density. G = -120, ψ_0 = 4, ρ_0 = 200, and τ = 1. Initial density 200 $mu\ lu^{-2}$ plus a random number in the interval [0,1]. Results shown at time = 0, 100, 200, 400, 800, 1600, 3200, 6400, 12800, and 25600 *ts*.

When phase separation occurs, there is a strong tendency for the interfaces formed to minimize their total area (or length in 2-D). This is a straightforward consequence of free energy minimization and occurs in part by geometric rearrangement into the minimum surface area volume (a sphere or in 2-D, a circle). Depending on the initial conditions, this rearrangement may also involve a significant amount of coalescence of 'blobs' of each phase. In liquid-vapor systems, there can also be condensation and evaporation; bubbles can simply fill in or grow at the expense of mass elsewhere in the domain. The relatively high vapor density in the simple simulations described in this book indicates a potential excess of transport in the vapor phase relative to many real liquid-vapor systems.

6.3.1 Spurious Interface Velocities

Examination of the velocity fields in SCMP simulations reveals high velocities perpendicular to phase boundaries. These are non-physical. They are present at equilibrium and there appears to be no mass exchange associated with them. Some papers that focus on or mention these velocities include Wagner (2003), Lishchuk et al. (2003), Nourgaliev et al. (2003), and Raiskinmäki et al. (2000).

6.3.2 Estimating Surface Tension

The surface tension can be estimated simply by simulating a series of drops and bubbles of various sizes and measuring their radii and inside/outside densities. The densities must be converted to pressures via the EOS and the difference ΔP computed. Then the slope of a plot of 1/radius vs. ΔP will be the surface tension in accordance with the Laplace law (Eq. (7)). Figure 47 presents results leading to a surface tension of 14.3 *lu mu ts*$^{-2}$. Readers are encouraged to develop such a plot on their own (see Exercises).

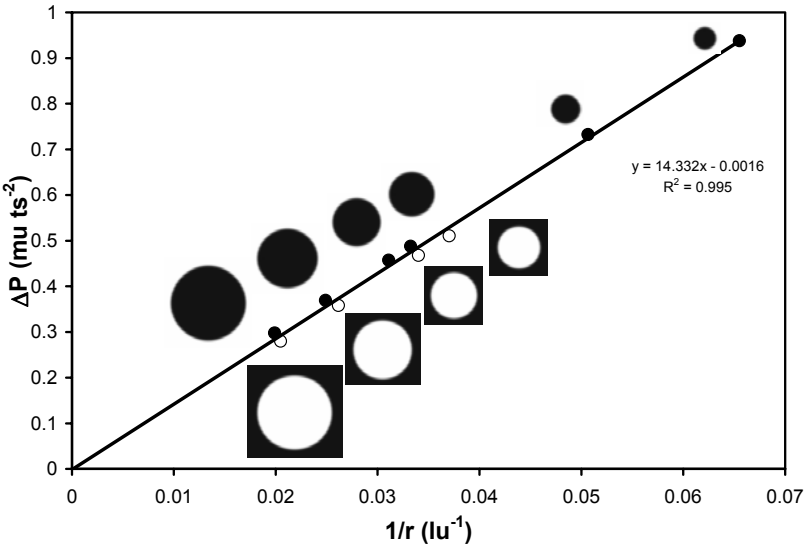

Figure 47. Plot of curvature (1/*r*) vs. pressure difference used to determine surface tension in SCMP lattice Boltzmann model. Simulated drops and bubbles shown adjacent to data points at relative scale. Bubbles consistently fall below line and drops are consistently above; this may be due to the selection of a density cutoff value for measuring radii.

6.3.3 Flat Interfaces: Maxwell Construction for SCMP LBM

Curved interfaces are common and the relationship between radii of curvature and pressure differential across them can be predicted when the surface tension is known. Flat interfaces are exceptionally important however because the vapor pressure above them at equilibrium is the saturation va-

por pressure, which is used in scaling many vapor pressure-dependent processes. At equilibrium, the pressure difference across a flat interface must be zero, which is consistent with the Laplace law, and the Maxwell Construction should apply. We have already illustrated a trial-and-error approach to solving the Maxwell Construction for the van der Waals equation of state. From more sophisticated numerical solutions of the Maxwell Construction on the SCMP LBM EOS with $\psi_0 = 4$, $\rho_0 = 200$, and $G = -120$, we compute $\rho_l = 514.64$ *mu* lu^{-2} and $\rho_v = 79.705$ *mu* lu^{-2}. These values differ appreciably from those observed in flat interface simulations that yield $\rho_l = 524.39$ *mu* lu^{-2} and $\rho_v = 85.704$ *mu* lu^{-2}. The observed vapor and liquid densities give very similar pressures of 25.5599 and 25.5605 respectively from the EOS, while the optimal Maxwell solution densities lead to pressures of 24.45172 and 24.45166. The reasons for this discrepancy are unknown and this represents a significant outstanding problem from our perspective. It may account wholly or in part for the less than quantitative results we obtain in certain types of simulations.

6.4 Cavitation

Cavitation is a catastrophic transition from liquid to vapor. Cavitation can be either 'homogeneous' when it occurs at the limit of the pure liquid's tensile strength, or 'heterogeneous' when it is nucleated by preexisting bubbles or other disruptions in the structure of the liquid. Single component multiphase lattice Boltzmann methods offer a virtual laboratory for investigation of cavitation.

Sukop and Or (2005) conducted LB simulations of cavitation in a two-dimensional geometry; they adapted Or and Tuller's (2002) discussion of three-dimensional critical bubble radius and energy cost for heterogeneous cavitation in 2-D. The energy cost for the creation of a vapor bubble is the sum of the interfacial energy needed to create the bubble and the work of negative pressure over the bubble area; that is,

$$\Delta E = 2\pi r\sigma + \pi r^2 \Delta P \tag{65}$$

with σ = (2-D) surface tension (MLT^{-2}), ΔP = (2-D) pressure (MT^{-2}), and r = bubble radius. This relationship is plotted in Figure 48. The energy cost is maximized at $r^* = -\sigma/\Delta P$. For any given tension applied to the LB system, r^* represents a critical bubble radius. A bubble with a radius less than r^* will be lost to condensation rather than result in cavitation because con-

densation is more energetically favorable. Once a bubble is large enough to overcome the energy barrier, cavitation is the more favorable outcome.

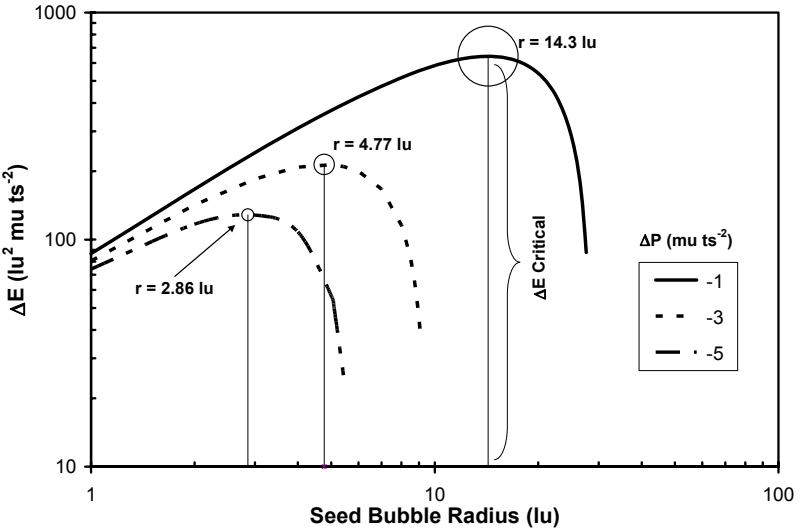

Figure 48. Energy barrier as a function of seed bubble radius for different initial liquid pressures. Circle size proportional to critical radii. ψ_0 = 4, ρ_0 = 200, and G = -120. (Sukop and Or, 2005)

6.4.1 Homogeneous Cavitation

Sukop and Or (2005) simulated spinodal decomposition (cavitation via homogeneous nucleation) in a 200×200 lu^2 domain. Figure 49 shows the process as the change in density at two points in the domain during the simulation. The initial density in the liquid is 400 $mu\ lu^{-2}$ (i.e., the liquid is under tension at the outset), but this simply hastens the process. The left and right boundaries are periodic, and constant velocity boundaries (0.005 $lu\ ts^{-1}$) at the top and bottom of the domain pull liquid from the domain. This results in increasing tension in the liquid with time until the liquid spinodal pressure and density are reached. Then the liquid cavitates catastrophically. Cavitation occurs as a linear band (lower left inset of Figure 49) in this simulation because there is no randomness in the pressure/density distribution in the domain and the vertical domain boundaries are periodic. In real systems, small fluctuations would result in random preferred loci of cavitation and bubbles would form. Severe den-

sity/pressure fluctuations occur in the liquid phase after the onset of cavitation; these eventually subside and liquid is present at density very close to its equilibrium, flat, free interface value of 524 *mu* lu^{-2}. Smaller fluctuations in the vapor phase are rapidly damped and a final density very close to the equilibrium value (85 *mu* lu^{-2}) is attained. The relative magnitudes of these fluctuations are consistent with the EOS and a greater compressibility in the liquid phase.

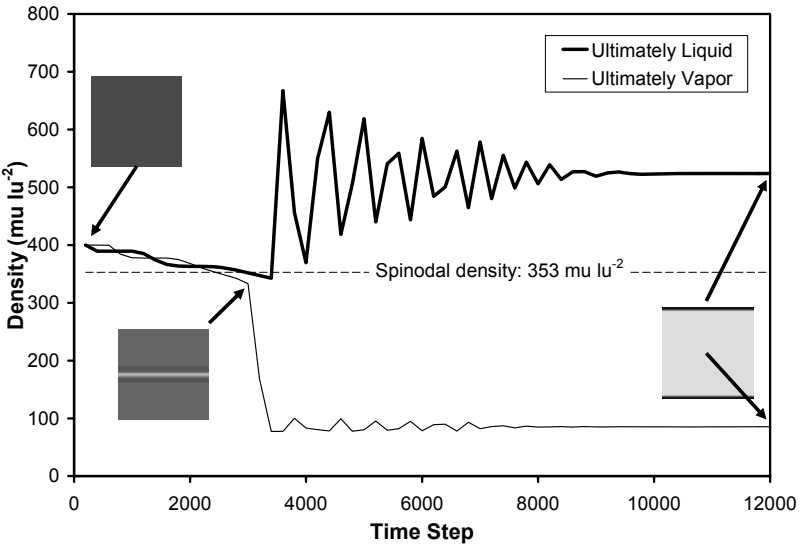

Figure 49. Density as a function of time for two points inside a 200 × 200 lu^2 domain. The fine line follows density at a point in the domain (100,100) that ultimately becomes vapor, while the heavy line gives the density near the boundary at a point (100,1) that is ultimately liquid. Insets show density distributions in domain. (Sukop and Or, 2005)

6.4.2 Heterogeneous cavitation

Sukop and Or (2005) also produced results that closely match heterogeneous cavitation theory (Or and Tuller, 2002). Periodic boundaries were used on the vertical edges of the 200×200 lu^2 domain and pressure boundaries were applied on the top and bottom. Based on the equation of state (Figure 45), the density of the vapor and liquid phases of the fluid can be calculated for any given pressure. A density corresponding to a liquid pressure below that of the experimental flat free interface was used on both bounda-

ries. (The difference between the boundary pressure and the pressure of a flat, free liquid-vapor interface is represented by ΔP in Figure 48.) These boundary conditions effectively stretch the fluid, creating a situation favorable for cavitation.

Sukop and Or (2005) inserted vapor bubbles of various sizes into their simulations. As shown in Figure 48, a bubble with radius just below the critical value cannot overcome the energy barrier and eventually condenses. However, a bubble with radius just above the critical value acts as a seed for cavitation. The LBM's proper simulation of these phenomena at two different liquid tensions is demonstrated in the following figures. In Figure 50, for ΔP = -1 *mu* ts^{-1}, the critical radius is 13.85 *lu* and the radii of the seed bubbles are 12 and 15 *lu*.

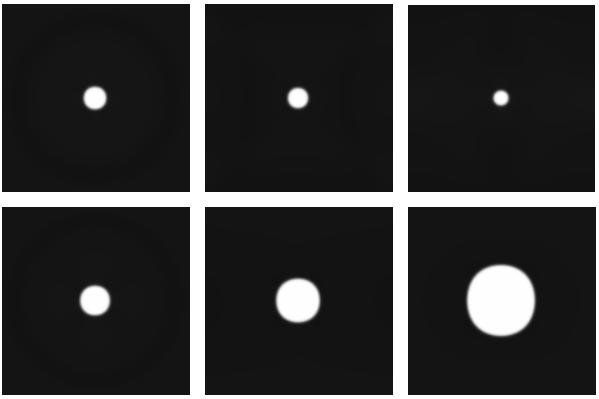

Figure 50. Effect of initial seed bubble size on evolution for ΔP = -1 *mu* ts^{-2}. Top: *r* = 12 *lu* bubble dissipates due to condensation. Bottom: *r* = 15 *lu* bubble nucleates cavitation.

Similarly, in Figure 51, for ΔP = -5 *mu* ts^{-1} the critical radius is 2.77 *lu* and the radii of the seed bubbles shown are 2 and 4 *lu*. Clearly, much smaller seed bubbles can nucleate cavitation at higher liquid tensions (more negative ΔP).

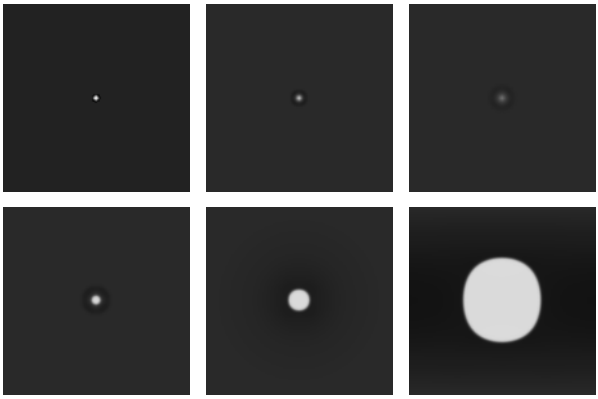

Figure 51. Effect of initial seed bubble size on evolution for ΔP = -5 *mu* ts^{-2}. Top: r = 2 *lu* bubble dissipates due to condensation. Bottom: r = 4 *lu* bubble nucleates cavitation.

6.5 SCMP LBM with Surfaces

6.5.1 Fluid-Surface Forces

In order to extend our capability to include simulation of SCMP fluids in porous media and other containers, it is essential that we incorporate an adhesive interaction between fluid particles and surfaces. The original method is due to Martys and Chen (1996) and is elegant in its simplicity. The idea is to create an analogue to the particle-particle interaction force used to induce phase separation. The only difference is that instead of summing the ψ functions of neighboring nodes (Eq. (60)), we sum an indicator variable denoting a solid. The strength of the force contribution is specified by a G_{ads} 'adsorption' coefficient. The equation describing this is

$$\mathbf{F}_{ads}(\mathbf{x},t) = -G_{ads}\psi(\mathbf{x},t)\sum_{a} w_a s(\mathbf{x}+\mathbf{e}_a\Delta t)\mathbf{e}_a \,, \tag{66}$$

where s is a 'switch' that takes on value one (1) if the site at $\mathbf{x} + \mathbf{e}_a\Delta t$ is a solid and is zero (0) otherwise. The w_a are the same direction-dependent weighting factors used before. The C implementation of Eq. (66) is straightforward. The `is_solid_node` array is used to evaluate if a node neighboring the fluid node under consideration is a solid; if so, a contribution is made to the surface force.

```
// Compute psi, Eq. (61).
for( j=0; j<LY; j++)
  for( i=0; i<LX; i++)
    if( !is_solid_node[j][i])
    {
      psi[j][i] = 4.*exp( -200. / ( rho[j][i]));
    }

// Compute interaction force, Eq. (66).
for( j=0; j<LY; j++)
{
  jp = ( j<LY-1)?( j+1):( 0   );
  jn = ( j>0   )?( j-1):( LY-1);

  for( i=0; i<LX; i++)
  {
    ip = ( i<LX-1)?( i+1):( 0   );
    in = ( i>0   )?( i-1):( LX-1);

    if( !is_solid_node[j][i])
    {
      sum_x=0.;
      sum_y=0.;

      if( is_solid_node[j ][ip]) // neighbor 1
      { sum_x = sum_x + WM*ex[1];
        sum_y = sum_y + WM*ey[1]; }
      if( is_solid_node[jp][i ]) // neighbor 2
      { sum_x = sum_x + WM*ex[2];
        sum_y = sum_y + WM*ey[2]; }
      if( is_solid_node[j ][in]) // neighbor 3
      { sum_x = sum_x + WM*ex[3];
        sum_y = sum_y + WM*ey[3]; }
      if( is_solid_node[jn][i ]) // neighbor 4
      { sum_x = sum_x + WM*ex[4];
        sum_y = sum_y + WM*ey[4]; }
      if( is_solid_node[jp][ip]) // neighbor 5
      { sum_x = sum_x + WD*ex[5];
        sum_y = sum_y + WD*ey[5]; }
      if( is_solid_node[jp][in]) // neighbor 6
      { sum_x = sum_x + WD*ex[6];
        sum_y = sum_y + WD*ey[6]; }
      if( is_solid_node[jn][in]) // neighbor 7
      { sum_x = sum_x + WD*ex[7];
        sum_y = sum_y + WD*ey[7]; }
      if( is_solid_node[jn][ip]) // neighbor 8
      { sum_x = sum_x + WD*ex[8];
        sum_y = sum_y + WD*ey[8]; }

      sforce_x[j][i] = -Gads * psi[j][i] * sum_x;
      sforce_y[j][i] = -Gads * psi[j][i] * sum_y;
    }
  }
}
```

We seem to have flexibility in the choice of the pre-sum factor $\psi(\mathbf{x},t)$; Martys and Chen (1996) originally used $\psi = \rho$, while Raiskinmäki et al. (2000; 2002) and Hyväluoma et al. (2004) used the ψ function $\psi(\rho) = 1 - \exp(-\rho)$. For consistency with the cohesion force, we use the ψ function Eq. (61) here.

Next we introduce a few studies that used the same basic Shan and Chen model we develop in this book and then give more detailed discussions of various phenomena in the following sections. Raiskinmäki et al. (2000) considered the spreading dynamics of three-dimensional droplets on surfaces with the Shan and Chen SCMP lattice Boltzmann model. They showed that the simulated rate of droplet spreading on a smooth surface was consistent with Tanner's Law, which states that the radius of the liquid/surface interface increases as a power function of time, $r \sim t^q$.

Raiskinmäki et al. (2002) investigated capillary rise dynamics using the same model. This work showed that the Washburn Equation, which predicts the rate of capillary rise, was satisfied by the SCMP LBM simulations. These authors concluded that relatively large capillary tubes – at least 30 lattice units across – would be needed to properly simulate the hydrodynamics. They also noted a discrepancy between the analytical Poiseuille velocity profile and the velocities of the liquid phase in an SCMP simulation; apparently the cohesive and adhesive forces imposed on the liquid affect its properties. Additional work needs to be done to assess this phenomenon.

Hyväluoma et al. (2004) also used the Shan and Chen SCMP LBM in an investigation of mercury intrusion porosimetry. In a similar study, Sukop and Or (2004) simulated contact angles, adsorption, capillary condensation, and wetting and drying of angular pores.

6.5.2 Contact Angles

Varying the G_{ads} parameter allows simulation of the complete range of contact angles. In Figure 52, we show SCMP simulations that yield 3 special contact angles: 0, 90, and 180 degrees.

We compute the necessary G_{ads} parameter for the three special contact angles by balancing the cohesive and adhesive forces in different ways. Assume that we are at points of either pure liquid or pure vapor. Then the

point's neighbors all have the same density as found at the point itself. From Eq. (60), the forces can then be written as

$$\mathbf{F} = -G\psi^2 \sum_{a=1}^{8} w_a \mathbf{e}_a \,, \tag{67}$$

where the ψs are all equal and can be combined. So, for the vapor and liquid phases respectively, we have

$$\mathbf{F}^v = -G\psi_v^2 \sum_{a=1}^{8} w_a \mathbf{e}_a \tag{68}$$

and

$$\mathbf{F}^l = -G\psi_l^2 \sum_{a=1}^{8} w_a \mathbf{e}_a \,. \tag{69}$$

A fluid node completely surrounded by solid surfaces would experience a different force. From Eq. (66) we obtain for vapor and liquid respectively:

$$\mathbf{F}_{ads}^v = -G_{ads}\psi_v \sum_{a=1}^{8} w_a \mathbf{e}_a \tag{70}$$

and

$$\mathbf{F}_{ads}^l = -G_{ads}\psi_l \sum_{a=1}^{8} w_a \mathbf{e}_a \,. \tag{71}$$

Note that the ψ factors are not squared here because the indicator variable *s* appears inside the summation rather than the ψ values.

We also consider the forces at points that have the average ψ value to represent the interface between liquid and vapor:

$$\overline{\mathbf{F}} = -G\overline{\psi}^2 \sum_{a=1}^{8} w_a \mathbf{e}_a \tag{72}$$

and

$$\overline{\mathbf{F}}_{ads} = -G_{ads}\overline{\psi}\sum_{a=1}^{8} w_a \mathbf{e}_a \,, \tag{73}$$

where

$$\overline{\psi} = \tfrac{1}{2}\left(\psi_\ell + \psi_v\right). \tag{74}$$

Note that all of the equations [(68) through (73)] contain the same summation term.

On a surface that is completely wetted by the liquid yielding a contact angle of 0 degrees, the adhesive force between the solid and the liquid is equal to the cohesive force of the liquid. Setting

$$\mathbf{F}^\ell = \mathbf{F}^\ell_{ads} \tag{75}$$

gives

$$-G\psi_l^2 \sum_{a=1}^{8} w_a \mathbf{e}_a = -G_{ads}\psi_l \sum_{a=1}^{8} w_a \mathbf{e}_a \,, \tag{76}$$

which reduces to

$$G_{ads} = G\psi_l \,, \tag{77}$$

For the usual liquid density (albeit a flat free interface value) of 524.39 *mu lu*$^{-2}$, $\psi = 2.7316$. The cohesion parameter has been selected as G = -120, so G_{ads} = -327.79. It is easy to check if this is reasonable with simulations. Figure 52 shows the results.

Figure 52. Simulation of 0, 90, and 180 degree contact angles based on the force balance rationale discussed in the text. For the cohesive interaction parameter G = -120 and the ψ function parameters ψ_0 = 4 and ρ_0 = 200, G_{ads} = -327.79, -187.16, and -46.534 respectively.

On a surface that is wetted by the liquid to an extent exactly between completely wettable and completely non-wettable for a contact angle of 90°, the adhesive force of the solid on the interface between liquid and vapor is equal to the cohesive force at the liquid-vapor interface. Setting

$$\overline{\mathbf{F}} = \overline{\mathbf{F}}_{ads} \tag{78}$$

leads to

$$G_{ads} = G\overline{\psi} = G\frac{(\psi_l + \psi_v)}{2}, \tag{79}$$

which gives G_{ads} = -187.16 for G = -120, ψ_l = 2.7316, and (with ρ_v = 85.70 *mu lu*^{2}) ψ_v = 0.38774.

Finally, on a surface that is completely non-wettable by the liquid for a contact angle of 180 degrees, the adhesive force between the solid and the vapor must equal the cohesive force of the vapor. Setting

$$\mathbf{F}^v = \mathbf{F}^v_{ads} \tag{80}$$

gives G_{ads} = -46.534 by the same procedure used for the 0-degree contact angle except that ψ_v = 0.38774 is the proportionality constant based on ρ_v = 85.70 *mu lu*$^{-2}$.

Readers should carry out similar simulations (see Exercises). Our experience suggests that it is easily possible to create zones of excessive density adjacent to surfaces with the magnitude of G_{ads} too large. This is probably another consequence of the lack of a repulsive interaction between the particles. The approach for selecting G_{ads} suggested here should make the process more rational than the trial-and-error procedure often followed. Our method is ad hoc however and questions remain on what is the most appropriate technique.

Considerable work on dynamic contact angles using LBM has also been completed (especially with the free-energy LBM; e.g., Zhang and Kwok, 2004; Raiskinmäki et al. 2002; Briant et al. 2002; Fan et al. 2001). A more fundamental basis and method for incorporating surface adsorption is needed (e.g., the various adsorption models discussed in Adamson and

Gast (1997) for example); nevertheless, reasonable results can be obtained. We demonstrate some applications in the following sections.

6.5.3 Capillary Rise

The SCMP LBM can be effectively used to simulate capillary rise in a simple capillary and by extension capillary rise phenomena in more complex porous media. The use of the dimensionless Bond number Bo – which relates capillary and gravitational forces – allows the simulation of direct analogues of real systems in the same way as the Reynolds number allowed the simulation of equivalent flow regimes.

We can adjust the surface adhesion parameter G_{ads} so that the desired contact angle is attained. For simplicity, we make the contact angle zero and we can use the 2-D Young-Laplace equation with a zero contact angle term to determine the pressure difference across a curved (2-D) interface:

$$\Delta P = \frac{\sigma}{r}. \tag{81}$$

With zero contact angle (and assuming there is no adsorbed liquid film), the interface radius of curvature is identical to the half-width of the 2-D capillary tube (a slit). For small capillaries in 3-D, Hyväluoma et al. (2004) have demonstrated that the ratio of capillary cross-sectional area to perimeter can account for discretization and is preferable to the radius for use in Eq. (81).

The hydrostatic pressure difference between the top and bottom of a column of incompressible liquid of height h in a gravitational field g is

$$\Delta P = \rho g h . \tag{82}$$

Equating the right hand sides of (81) and (82) gives

$$\rho g h = \frac{\sigma}{r}, \tag{83}$$

which can be rearranged as the capillary rise equation:

$$h = \frac{\sigma}{r\rho g}. \tag{84}$$

The dimensionless Bond number reflects the balance between gravitational and capillary forces and is

$$Bo = \frac{r^2 \rho g}{\sigma}. \tag{85}$$

Bo is effectively r/h. To illustrate its use in defining an LBM capillary rise arrangement equivalent to a real capillary system, we consider a real capillary slit 0.002 *m* in width ('radius' = 0.001 *m*) in contact with a pool of water with density 1000 $kg\ m^{-3}$ and gravity $g = 9.8\ m\ s^{-2}$. The surface tension of water is $72.13\times10^{-3}\ Nm^{-1}$. Solving for the capillary rise we obtain

$$h = \frac{72.13\times10^{-3}\,Nm^{-1}}{0.001\,m\,10^{3}\,kg\,m^{-3}\,9.8\,m\,s^{-2}} = 7.36\times10^{-3}\,m. \tag{86}$$

Now we can compute the Bond number for the real system: Bo = r/h = 1/7.36. Defining an analogous LBM system can begin with a domain size. Say that the maximum capillary length and rise we wish to simulate is on the order of 300 *lu*. From the Bond number, $r = h$ Bo, and in our specific case the radius r = 300 *lu*/7.36 = 41 *lu*.

We still need to incorporate the density of the LBM liquid and determine a gravity value to use in the simulation. Rearranging Eq. (84) we can solve for *g* as

$$g = \frac{\sigma}{r\rho h} \tag{87}$$

or $g = 2.222\times10^{-6}\ lu\ ts^{-2}$ for our model problem. We chose a domain size of $1000\times600\ lu^2$ with a wall on the bottom and $\tau = 1$ (preliminary observations suggest that the rise might be affected by τ, but we have not investigated this). To expedite the computer run we begin with the capillary filled to the approximate rise height from an initially flat liquid/vapor interface at $y = 180\ lu$. The results are shown in Figure 53. The simulated rise of 334 *lu* is about 10% greater than the target value of 300 *lu* computed analytically above. In part this is due to the presence of a non-negligible wetting

film (Langmuir 1938) with a thickness of approximately 3 *lu* on the capillary walls. Recomputing the expected rise with Eq. (84) and a effective capillary radius of 38 *lu* together with the observed average liquid density in the capillary (523.5 *mu* lu^{-2}) yields 324 *lu* – still an approximation.

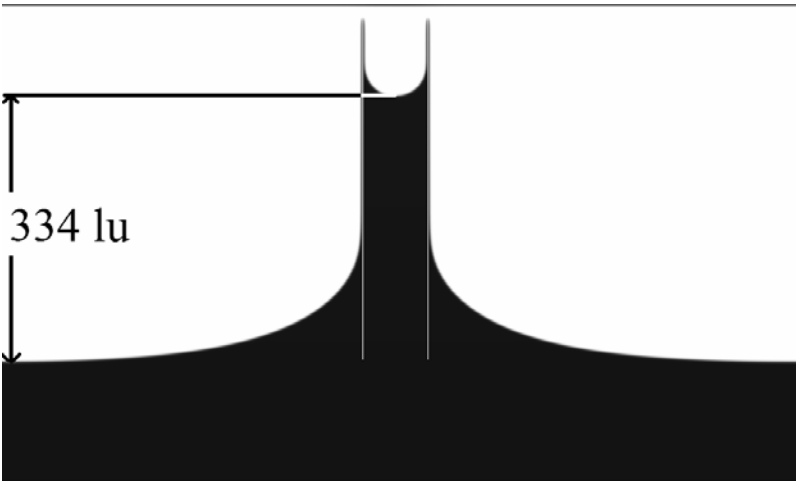

Figure 53. Capillary rise in a 1000×600 lu^2 domain at 81,000 *ts*. Density of fluid shown as gray scale. Capillary walls in white. Dark edges show wetting film.

As discussed in relation to the SCMP EOS, the model we use simulates compressible liquid and gas phases. The liquid phase is actually more compressible than the gas phase.

The hydrostatic pressure difference between the top and bottom of a column of *compressible* fluid of height h in a gravitational field *g* under isothermal conditions is approximately (Halliday and Resnick, 1978)

$$\Delta P = P_0\left(e^{\rho_0 gh/P_0} - 1\right). \tag{88}$$

Here ρ_0 and P_0 are the density and pressure at some reference level in the fluid. We can set the ΔP on the left side of Eq. (88) to the ΔP from the Young-Laplace equation (81) and rearrange to have a capillary rise equation for compressible fluids:

$$\frac{\sigma}{r} = P_0\left(e^{\rho_0 gh/P_0} - 1\right) \Rightarrow$$
$$h = \frac{P_0}{\rho_0 g}\ln\left(\frac{\sigma}{P_0 r} + 1\right), \tag{89}$$

where a zero contact angle has been assumed. If the reference density is the flat, free interface value of 524.39 *mu* lu^{-2} inside the capillary slit at the level of the free liquid pool outside the slit, then the reference pressure is 24.66 from the EOS. Considering again the effective half-width of the slit due to the adsorbed liquid film, we compute a capillary rise of 329 *lu*, which is reasonably close to the simulated result.

Thus we have several possible strategies; we can ensure that g remains small and that fluid compression is negligible or we can account for the compressibility. The first approach was used by DiPietro et al. (1994) in an early lattice gas simulation of capillary phenomena. Hyväluoma et al. (2004) used an integrated density through the liquid to remove the effect of the compressibility. The above analysis incorporating the compressibility is probably more fundamental and should apply to a broader range of parameters, but we have not investigated it further.

6.5.4 Adsorption/Capillary Condensation

Important phenomena that occur when a vapor phase interacts with a surface include adsorption and capillary condensation. Adsorption is the accumulation of the vapor phase chemical on the solid surface. This accumulation will commonly result in surface condensation and the formation of a liquid film. Numerous physicochemical processes can be responsible for the formation of such films, but if one limits consideration to ubiquitous van der Waals interactions (Tuller et al. 1999), then as a first approximation the thickness of the film formed is a function of the vapor pressure and a Hamaker constant A_{slv} that quantifies the interaction of the solid surface with vapor through a liquid film.

$$h(\Pi) = \sqrt[3]{\frac{A_{slv}}{6\pi\Pi}}\,. \tag{90}$$

Here Π is the disjoining pressure (P relative to flat, free interface).

When films on opposing surfaces grow towards one another – such as on opposite walls of a pore – a critical film thickness is reached beyond which the pore spontaneously fills completely. The critical thickness is approximately H/3 where H is the aperture width. The equation governing the simultaneous growth of the films on opposing surfaces is an extension of Eq. (90):

$$\Pi = \frac{A_{slv}}{6\pi h^3} - \frac{A_{lvl}}{6\pi\left(H-2h\right)^3} + \frac{A_{slv}}{6\pi\left(H-h\right)^3}, \tag{91}$$

where A_{lvl} is a new Hamaker constant that governs the interaction of liquid with liquid through an intervening vapor phase. It is possible to estimate the values of the Hamaker constants by fitting Eqs. (90) and (91) to simulations. With 1 or 2 adjustable parameters these are rather inflexible equations however and good fits using the current LBM are elusive. Simulations of film adsorption and capillary condensation with the SC LBM model have not been widely reported in the literature – probably because of difficulties in obtaining satisfying results. Sukop and Or (2003) presented some promising preliminary results using a different form of the adhesive force (Figure 54), but our current, presumably improved code does not seem to simulate these particular phenomena as well. More detailed analysis of the nature of the approximation of surface forces in LBM is needed.

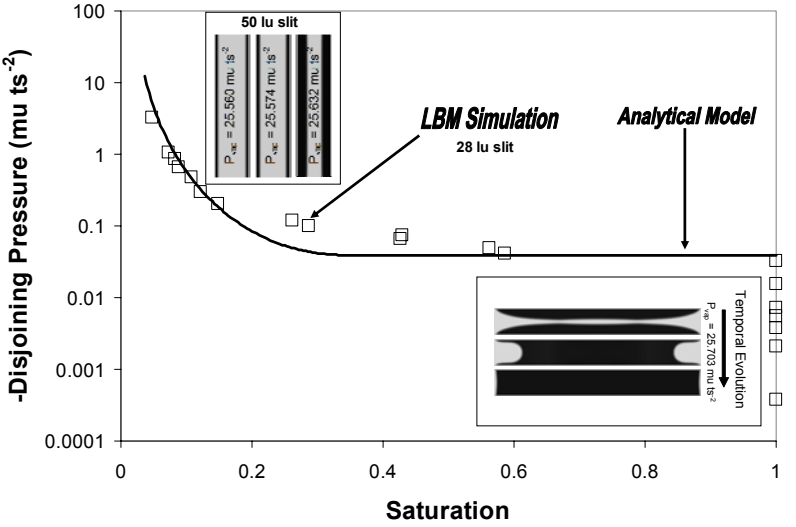

Figure 54. Simulation of film adsorption and capillary condensation from Sukop and Or (2003). The surface force Eq. (66) used the density rather than the ψ function and was not divided by the density as Eq. (47) requires.

6.5.5 Hysteretic Wetting/Drying of Porous Media

Despite challenges with the detailed surface adsorption and capillary condensation simulations, LBM has been used successfully to simulate the hysteretic wetting and drying of porous media. We refer readers to Pan et al. (2004) and Vogel et al. (2005) for 3-D examples.

6.5.6 Fluid Displacement in Porous Media

The displacement of one fluid by another in porous media leads to a rich variety of behaviors depending on the properties of the fluids, the rate of displacement, gravitational effects, and the structure of the medium. Lenormand (1988) condensed the fluid properties and displacement rate into two parameters and showed the variety of behaviors experimentally. As we have seen previously for other fluid phenomena, such observations present opportunities for validation of lattice Boltzmann methods. We present Lenormand's results and some early attempts at simulating such be-

havior with LBM here (Sukop and Or 2003); more advanced efforts should follow.

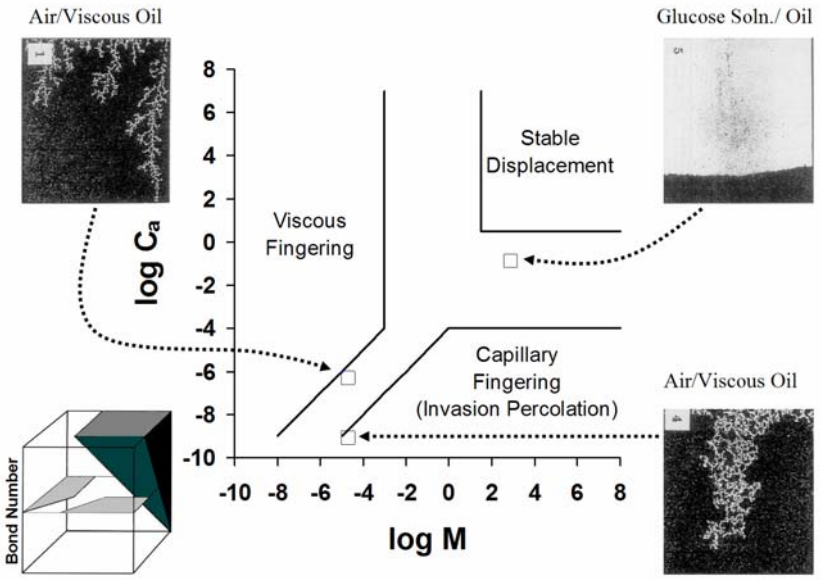

Figure 55. Fluid displacement phase diagram and displacement patterns adapted from Lenormand et al. (1988) with permission of Cambridge University Press. The displacement fronts have different characteristic shapes depending on the Capillary number Ca and the viscosity ratio *M*. The inset on the lower left shows that the 'stable displacement' field expands as the Bond number increases (Berkowitz and Ewing, 1998).

The Capillary number (Ca) is a dimensionless number that gives the relative magnitude of viscous and capillary forces. It can be stated as (Friedman, 1999):

$$Ca = \frac{u\mu}{\phi\sigma\cos\theta} \tag{92}$$

with u the inlet/outlet velocity, μ the viscosity of injected fluid, porosity ϕ, interfacial tension between fluids σ, and contact angle θ. Under many conditions, the other variables are fixed and the Capillary number can be considered a measure of velocity.

The second key variable considered by Lenormand is the ratio (M) of the viscosities of the injected and displaced fluids:

$$M = \frac{\mu_{injected}}{\mu_{displaced}} \tag{93}$$

While this ratio can be varied freely in experimental work by choosing appropriate fluid pairs, this is less straightforward in simple LBM models. For the D2Q9 SCMP model, we find

$$M = \frac{\frac{c^2}{3}\left(\tau - \frac{\Delta t}{2}\right)\rho_{injected}}{\frac{c^2}{3}\left(\tau - \frac{\Delta t}{2}\right)\rho_{displaced}} = \frac{\rho_{injected}}{\rho_{displaced}} \cong 0.1 \tag{94}$$

which indicates that the viscosity ratio is controlled by the density ratio when τ is held constant. For the parameters used for SCMP throughout this text, the ratio of vapor to liquid density is on the order of 0.1; far greater density contrasts are generally the norm in the physical world. Similarly to the non-physical relative compressibilities of the liquid and vapor phases noted above, these fixed density and viscosity ratios are not a significant drawback for the computation of equilibrium interface configurations; in fact equilibrium conditions may be attained more quickly due to significant mass transport in the vapor phase. These ratios can affect numerous other phenomena of interest however, and the desire to vary the viscosity ratio to simulate these displacement processes is a good example.

A few strategies are available for varying the viscosity ratio. Ultimately, incorporation of a real equation of state would give the true density contrast. A more immediate approach would be to simply change the EOS parameters to increase the density contrast. This can lead to numerical instabilities however. A second approach is to vary τ as a function of density (Tölke et al. 2002; Nie et al. 1998). We have not experimented with this in the context of SCMP models yet, but successfully use it to simulate the flow of immiscible fluids below.

Single component multiphase lattice Boltzmann methods were applied to invasion percolation in simplified porous media by Sukop and Or (2003). They demonstrated the invading fluid's selectivity for the largest available pore and showed how this is affected by Ca. These abilities are crucial to

simulation of behavior in larger networks. To simulate these displacement processes, Sukop and Or (2003) induced interface movement from a phase-separated initial condition with fixed velocity (u_y = constant, u_x = 0) boundary conditions at the vapor inlet and liquid outlet in keeping with the typical experimental practice of constant flow rate. They maintained constant equal volumetric fluxes at the inlet and outlet. Since the (2-dimensional) volume of the fluid injected per unit time is the velocity multiplied by the inlet length, equal volumetric fluxes in the vapor and liquid correspond to equal velocities in the two phases. Implementation of the constant velocity boundary conditions followed the approach proposed by Zou and He (1997).

Figure 56 shows invasion of injected vapor phase through a perforated plate with holes of varying size. In the upper time sequence of images at low Ca; only the largest pore is invaded. In contrast, the bottom sequence shows invasion of the 2 largest pores at larger Ca when viscous effects become more important. These results are similar to those obtained by An-

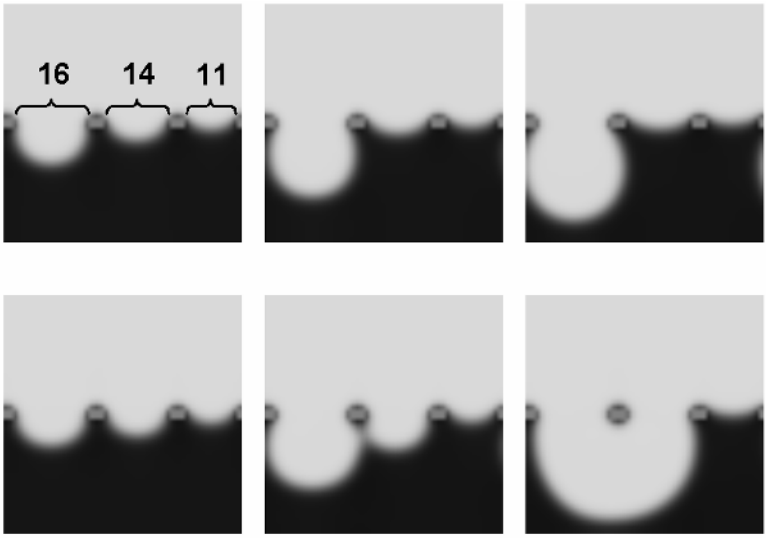

Figure 56. Time series (left to right) of invasion of vapor through plate with perforations of 16, 14, and 11 *lu*. Ca = 10^{-3} (top) and Ca = 10^{-2} (bottom). Liquid black, vapor gray, solids dark gray. (Sukop and Or, 2003) At low Capillary number, capillary forces dominate and only the largest pore is invaded by vapor. Increasing the Capillary number (displacement velocity in this case) causes a second pore to be invaded despite its smaller size.

gelopoulos, et al. (1998) with the free energy lattice Boltzmann model; selectivity for the largest pore was demonstrated but the effect of Ca was not investigated in that work.

Figure 57 illustrates the effects of changes in Ca in a network of pores. Each simulation is carried out on a 200×200 lattice with the same random arrangement of disks of three different sizes. For the disks, r = 2.5, 3.5, or 4.5 *lu*. The domains are periodic in the x direction, although disks at the left and right edges of the domain are fixed at large size and effectively bound the invasion process. Results near breakthrough for two Ca are shown. There are significant differences in the invasion patterns as a function of Ca.

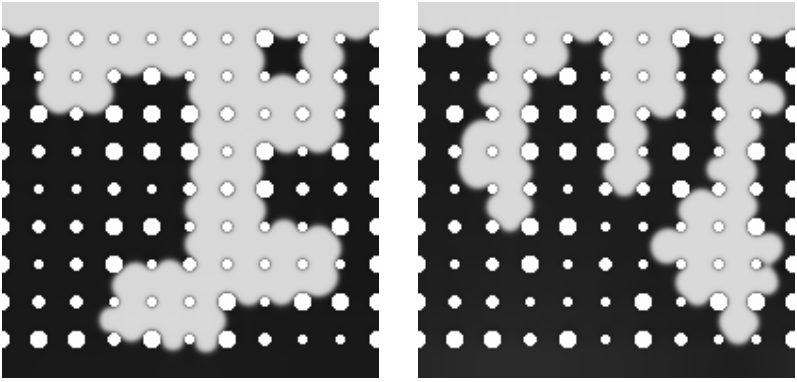

Figure 57. Vapor invasion into a porous medium consisting of random disks at two Capillary numbers. Ca = 10^{-3} (left) and Ca = 10^{-2} (right). Liquid black, vapor gray, solids white.

As noted in the caption of Figure 55, gravity can play a role in stabilizing (flattening) a fluid invasion front at certain Bond numbers when the displaced fluid is denser and tends to collect at the bottom of the domain. Figure 58 illustrates the effect.

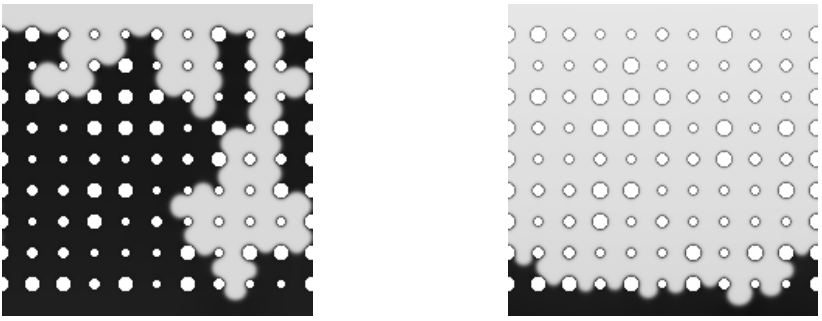

Figure 58. Effect of gravity on displacement front. The front is ramified in the absence of gravity (left). Gravity stabilizes front when the invading fluid is less dense (right). Liquid black, vapor gray, solids white.

6.6 Exercises

1. Plot a family of curves of ρ vs. P for different G (0, -80, -100, -120, and -140). Use $\psi_0 = 4$, $\rho_0 = 200$ mu lu^{-2}.

2. Use the Maxwell Construction to estimate the equilibrium vapor pressure from an equation of state with G = -120 and the ψ function parameters $\psi_0 = 4$ and $\rho_0 = 200$ mu lu^{-2}.

3. Simulate a flat interface in a fully periodic domain by beginning with an initial condition with density 500 *mu lu*$^{-2}$ in half of the domain and density 80 *mu lu*$^{-2}$ in the other half. Use the same parameters as in Exercise 2. Run the model to equilibrium and measure the equilibrium densities. Compute the pressure in each phase using the EOS and comment on your results.

4. Simulate drops and bubbles of various sizes in a fully periodic domain by starting with different initial densities in the unstable portion of the EOS (seeds or randomness in the initial density distribution may be necessary to prevent a metastable situation). Measure the drop and bubble diameters and the inside and outside densities. Convert the densities to pressures using the EOS. Plot the pressure difference (high – low) as a function of the inverse radii (the curvature), fit a line and estimate the surface tension. Track and report all units.

5. Compute the critical radius for heterogeneous cavitation under an initial fluid tension of -2 *mu* ts^{-1}. Use the LBM model to simulate the fate of bubbles of size greater than and less than the critical radius.

6. Simulate different contact angles by adding a surface and varying G_{ads}. It is helpful to start with a liquid 'blob' near the surface. Plot the density profile through the vapor, liquid, and solid.

7. The water-water vapor surface tension is 72.13×10^{-3} $N\ m^{-1}$ at 25C. Compute the capillary rise in a clean glass slit of radius 0.001 *m* in the Earth's gravitational field. We choose a slit to reduce the problem to a 2 dimensional one, in which there is only one possible radius of curvature. Assume the contact angle is zero. Show all units.

8. Compute the Bond number for the capillary rise problem above.

9. Propose and run a lattice Boltzmann model illustrating capillary rise at the Bond number found in Exercise 8. Remember that *r* should be at least 5 or so lattice units and that the 'pool' of liquid that the capillary will be immersed into should be wide enough that a pool height unaffected by capillary rise can serve as a reference level for measuring the liquid rise in your capillary. What is the expected capillary rise in your model? Show all calculations and units. Remember to use a surface adhesion parameter that corresponds closely to the desired contact angle; too big or too small may cause problems. Plot the steady-state result of your model. What is the observed capillary rise? Compare the ratio *h*/*r* for the case on Earth, the predicted LB case, and the simulated case.